SATELLITE PARALLAXES OF LENSING EVENTS TOWARD THE GALACTIC BULGE

B. Scott Gaudi and Andrew Gould[1]

Department of Astronomy, Ohio State University, Columbus, OH 43210;
gaudi@payne.mps.ohio-state.edu, gould@payne.mps.ohio-state.edu

ABSTRACT

In order to understand the nature of the lenses that generate microlensing events, one would like to measure their mass, distance, and velocity. Unfortunately, current microlensing experiments measure only one parameter of the events, the characteristic timescale, which is a combination of the underlying physical parameters. Other methods are required to extract additional information. Parallax measurements using a satellite in an Earth-like orbit yield the projected velocity of the lens: $\tilde{v} = v/(1 - z)$, where v is the transverse velocity (speed and direction) of the lens relative to the Earth-source line of sight, and z is the ratio of the distances to the lens and the source. A measurement of $\tilde{v}$ could distinguish between lenses belonging to the bulge and disk populations. We show that for photometric precisions of 1%–2%, it is possible to measure the projected speed, $\tilde{v}$, to an accuracy of $\leq 10\%$ for over 70% of disk lenses and over 60% of bulge lenses. For measuring the projected velocity $\tilde{v}$, the percentages are 40% and 30%, respectively. We find lines of sight greater than 2° away from the ecliptic are preferable, and an Earth-satellite separation in the range 0.7 AU–1.9 AU is optimal. The requirements of the satellite for measuring the projected velocities of events toward the bulge are similar to those for measurements toward the LMC.

Subject headings: astrometry — Galaxy: stellar content — gravitational lensing

1. INTRODUCTION

Four ongoing microlensing searches have detected more than 100 candidate events, the great majority toward the Galactic bulge. The MACHO collaboration (Alcock et al. 1995b, 1996b) have reported eight candidate microlensing events of stars in the Large Magellanic Cloud (LMC), more than expected by the known luminous stars of the Milky Way (Bahcall et al. 1994; Gould, Bahcall, & Flynn 1996) and LMC (Gould 1995b), but less than expected from standard spherical halo models (Paczyński 1986; Griest 1991). The EROS collaboration (Aubourg et al. 1995; Ansari et al. 1996) have reported two candidate events toward the LMC. The MACHO (Alcock et al. 1995a, 1996a), OGLE (Udalski et al. 1994), and DUO (Alard 1996) collaborations have reported more than 100 candidate events of stars toward the Galactic bulge. This is also more than expected by known stars. These discrepancies suggest that a revision of the current models of the structure of the disk, bulge, and halo may be in order.

The light curve generated by a microlensing event is described by the magnification $A(x) = (x^2 + 2)/x(x^2 + 4)^{1/2}$, where $x(t)$ is the position of the lens in the Einstein ring as a function of time, and is given by $x(t) = [\omega^2(t - t_0)^2 + \beta^2]^{1/2}$. Here t_0 is the time of maximum magnification, β is the impact parameter in units of the Einstein ring radius, and $\omega = t_e^{-1}$ is the inverse Einstein ring crossing time. Thus the magnification curve is fitted by three parameters, ω, β, t_0. Of these three parameters, only ω yields any information about the lens itself; β and t_0 reflect only the geometry of the event. The timescale is related to the Einstein ring radius and velocity of the lens by $t_e = r_e/v$. Here $v = |v|$ is the magnitude of the transverse velocity of the lens along the

Earth-source line of sight,

$$v = v_l - \left(v_s \frac{d_{ol}}{d_{os}} + v_o \frac{d_{ls}}{d_{os}} \right), \qquad (1.1)$$

where v_s, v_l, and v_o are the transverse velocities of the source, lens, and observer, respectively, d_{ol} and d_{os} are the distances to the lens and source, and d_{ls} is the distance between the lens and the source. The Einstein ring radius is defined as

$$r_e^2 = \frac{4GM}{c^2} d_{os} z(1 - z), \quad z = \frac{d_{ol}}{d_{os}}. \qquad (1.2)$$

Thus the timescale is a combination of the lens's physical characteristics: M, d_{ol}, and v. Because the bulge and disk of the Galaxy are characterized by different speed and distance distributions, separate measurements of v and d_{ol} would allow one to determine the component to which the lens belongs. Measurement of M would yield the mass spectrum of lenses in these components. Unfortunately, a measurement of t_e alone provides no direct information about these characteristics. Some information can be obtained by considering probability distributions, but this method is inherently statistical in nature. Furthermore, lenses belonging to the Galactic bulge will produce events with timescales very similar to those produced by lenses belonging to the Galactic disk. As a result, measurements of t_e alone differentiate poorly between these two components.

In order to discriminate between the bulge and disk components, one must consider methods of extracting more information from each event. Several methods have been proposed, including using parallax to measure the projected velocity of the lens, $\tilde{v} \equiv v/(1 - z)$. There are two basic methods of acquiring information from parallax: ground-based measurements and space-based measurements. The projected velocity of one lens has already been measured

using ground-based parallax (Alcock et al. 1995c). However, ground-based parallax is limited to those events for which the crossing time is large, $t_e \gtrsim 2$ months; it is only for these events that the motion of Earth induces measurable asymmetries in the light curve. Unfortunately, most of the events that have been detected so far have timescales significantly smaller than those required for ground-based parallax.

Ground-based parallax illustrates a generic problem inherent in most of the methods that have been proposed for measuring the physical characteristics of lenses. These methods are effective only for a small fraction of events. Furthermore, those events for which these methods are viable typically represent a very biased subsample. Measurements of proper motions are biased toward bulge events, color-shift measurements are biased toward bright lenses, and ground-based parallax measurements are biased toward events with long durations. In contrast, satellite-based parallax measurements are effective for a majority of events and are not biased toward a particular class of events.

Two basic methods have been suggested of measuring the proper motion of the lens, $\mu = v/d_{\mathrm{ol}}$. These are photometric (Gould 1994; Nemiroff & Wickramasinghe 1994; Witt & Mao 1995; Witt 1995; Loeb & Sasselov 1995; Gould & Welch 1996) and spectroscopic (Maoz & Gould 1994). Ideally one would like to combine measurements of both the proper motion and the parallax to determine both $\tilde{v}$ and μ. These two parameters, along with the timescale, completely determine M, d_{ol}, and v (Gould 1996). (Combined measurements of the proper motion and parallax can be used to determine the true velocity of the lens only if the projected velocity, $\tilde{v}$, is determined, and not just the projected speed $\tilde{v}$.) As we discuss below, parallax measurements can be used to determine $\tilde{v}$ in a significant fraction of events. Thus the mass spectrum, physical distribution, and velocity distribution of lenses could be determined if both the parallax and proper motion of events could be measured. Unfortunately, while optical interferometers may be able to measure proper motions for many events in the relatively near future, events for which proper motion can currently be measured are rare.

It is not strictly necessary, however, to measure both μ and $\tilde{v}$ in order to distinguish between component populations of lenses. Han & Gould (1995) demonstrated that, for events toward the Galactic bulge, the typical values of $\tilde{v}$ are reasonably well separated. Thus a measurement of $\tilde{v}$ alone, gathered from parallax information, can be used to determine the component to which the lens belongs. Furthermore, parallax measurements can often be used to determine not only $\tilde{v}$, but also the projected velocity of the lens, $\tilde{v}$. Information about v is even more useful in distinguishing between bulge and disk populations (Han & Gould 1995).

Space-based parallax is the most promising method of extracting information about lenses. Gould (1995a) demonstrated the basic method of using information obtained by a satellite in an Earth-like orbit to measure $\tilde{v}$, and also gave a rough estimate of the photometric precision needed. Due to parallax, the light curve of a particular microlensing event will be different as seen from Earth and the satellite. This difference is given by the vector displacement of the lens in the Einstein ring, $\Delta x \equiv (\omega \, \Delta t, \Delta \beta)$. Here Δt is the difference between the time of maximum magnification for the Earth and satellite, $\Delta t = t'_0 - t_0$, and $\Delta \beta$ is the difference between

the impact parameters, $\Delta \beta = \beta' - \beta$. The vector displacement is related to the Earth-satellite separation by

$$\Delta x = \frac{r}{\tilde{r}_e}, \qquad (1.3)$$

where r is the projection of the Earth-satellite separation vector R, onto the plane of the sky (perpendicular to the source vector $\hat{s}$), and $\tilde{r}_e$ is the projected Einstein ring radius,

$$\tilde{r}_e = \frac{r_e}{1 - z}. \qquad (1.4)$$

Thus by measuring t_0 and β for Earth and the satellite, one can determine the projected Einstein ring radius, and this, combined with the timescale t_e, can be used to calculate the projected velocity of the lens, $\tilde{v}$.

Complications arise from the fact that there is a fourfold degeneracy inherent in the determination of $\tilde{v}$, including a twofold degeneracy in the projected speed, $\tilde{v}$. These degenerate cases arise from the fact the one does not know a priori which side of the lens-source line the Earth and the satellite are on. Thus $\Delta \beta$ can have two magnitudes, $\Delta \beta_{\pm} = |\beta' \pm \beta|$, and two distinct signs, $\pm \Delta \beta_{\pm} = \pm |\beta' \pm \beta|$, for a total of four degenerate cases. This degeneracy can, in principle, be broken by measuring the small difference in inverse timescales, $\Delta \omega = \omega' - \omega$, caused by the relative velocity of Earth and the satellite (Gould 1995a).

Launching a satellite for observing microlensing would be a major undertaking. It is often suggested that the most economical approach would be to attach the telescope to an already planned mission. It turns out, however, that the stability requirements for observations of microlensing events are such that it would be more economical to launch a dedicated satellite. The primary concern, therefore, is that such a dedicated satellite would be sufficiently versatile and beneficial to justify the expense. We have already discussed what could be gained from a measurement of $\tilde{v}$ of lenses, but it remains to be shown that a satellite with reasonable specifications will actually enable one to measure $\tilde{v}$, and whether these measurements could be made for a large class of microlensing events. There is the further consideration that there are two distinct lines of sight of microlensing observations, the LMC and the Galactic bulge. The times of year when these two lines of sight can be observed from the ground are complementary, and one would like one satellite to be able to make measurements for both cases. Since the two cases are markedly different in the nature of events that are expected, the brightness of the source stars being observed, and in the geometry of the parallax measurements, it is not obvious that a satellite with specifications suited to LMC parallax measurements will also be able to make parallax measurements toward the Galactic bulge.

It is interesting to ask what the required lifetime of a parallax satellite would be to achieve a reasonable statistical sample of microlensing events. Gould (1995a) estimated that ~ 100 giant star events will be seen toward the bulge during each ~ 6 month bulge season. To observe each event 80 times requires observing ~ 44 events per day, or one event every ~ 30 minutes. The source stars will be typically $I \lesssim 17$, thus to achieve 2% photometry requires observations of ~ 10 minutes on a 25 cm telescope. It is therefore possible to make measurements with 2% photometry for all ~ 100 events. As we discuss below, it is possible

to measure the projected speed for $\sim 70\%$ of these events. Gould (1996) estimates that $\sim 15\%$ of giant events could yield measurements of the proper motion, μ. Thus for a satellite lifetime of 3 yr, we could expect to use combined parallax and proper motion information to measure the mass and distance of ~ 45 lenses.

In our analysis, we choose to assume that the satellite is on an Earth-like orbit, separated from Earth by a distance d_{sat}. As we show in the Appendix, this orbit well approximates a realistic orbit in which the satellite has a small velocity relative to Earth at the time of launch. Such an orbit is attractive on practical grounds since it requires the least amount of energy to attain. Other orbits, such as those inclined to the ecliptic plane, or with highly eccentric orbits, require a much larger velocity relative to Earth at the time of launch, and are therefore more expensive to achieve. An Earth-like orbit is therefore optimal for the analysis because it is simplest to study and is the most feasible. As we demonstrate below, such an orbit is also advantageous because it allows for parallax measurements toward the LMC and bulge equally well.

In a earlier paper, Boutreux & Gould (1996) used Monte Carlo simulations of observations of microlensing events in the direction of the LMC to determine the conditions needed to measure the projected speed, $\tilde{v}$ and the projected velocity, $\tilde{\boldsymbol{v}}$. They found that with photometric precisions of 3% for Earth and 4% for the satellite, and an Earth-satellite separation of greater than 0.5 AU that it was possible to measure $\tilde{v}$ for 70% and $\tilde{\boldsymbol{v}}$ for 50% of LMC events. They found that larger d_{sat} was preferable, and that parallax measurements were possible for a broad range of lens masses.

In this paper, we extend the Monte Carlo analysis of Boutreux & Gould (1996) to observations of microlensing events in the direction of the bulge in order to determine if similar satellite requirements are needed for bulge and LMC observations. We have determined the conditions needed to break the degeneracy for a majority of events, and thus to measure the projected speed, $\tilde{v}$, and the projected velocity, $\tilde{\boldsymbol{v}}$ to an accuracy of $\leq 10\%$. We consider the effects of the satellite requirements, the photometric precision and Earth-satellite separation, as well as the mass of the lens and the position of the source star, in order to ensure that the parallax measurements will be sensitive to a broad class of events. We also consider the time of year the observations are made, which, as we show, is a critical parameter for bulge observations. As we discuss in § 2.4, it is predominantly for this reason that the analysis of bulge observations is substantially more complicated than that of LMC observations. The reader may wish to review Boutreux & Gould (1996) in order to become familiar with a similar problem in a simpler setting.

2. MEASURING $\tilde{\boldsymbol{v}}$

The ability to measure $\tilde{\boldsymbol{v}}$ is dependent on a number of different parameters, several of which are tied together in intricate ways. In this section, we define these parameters and use a qualitative comparison between observations toward LMC and observations toward the bulge to explain how these parameters affect measurement of the projected velocity. In § 3 we justify these ideas mathematically. We quantify the ability to measure $\tilde{\boldsymbol{v}}$ by introducing the degeneracy breaking fraction (DBF). The DBF can be thought of as the percentage of events for which the projected velocity

can be measured to an accuracy of $\leq 10\%$ for a specified set of the independent parameters.

In order to measure the projected velocity, one must be able to break the degeneracy between the four possible solutions. We formulate a constraint (derived from the difference in inverse timescales) and discard those solutions which do not obey this constraint. We require that those solutions allowed by the constraint have fractional errors which are small and are close enough that their difference is unimportant. If these requirements are met, we consider the degeneracy broken. We discuss the DBF quantitatively in § 2.3.

2.1. Constraint Condition

We distinguish the four discrete solutions by means of a constraint on the observables, Δt, $\Delta \beta$, and $\Delta \omega$. Here $\Delta \omega \equiv \omega' - \omega$ is the difference in inverse timescales between the satellite and Earth. Those solutions that are disallowed by the constraint at the 3 σ level are distinguishable. As we show below, the ability to break the degeneracy is complicated by the fact that the constraint coefficients are strong functions of the time of year.

The constraint is (Gould 1995a)

$$u_{\parallel}\,\omega\,\Delta t + u_{\perp}\,\Delta \beta - r\,\Delta \omega = 0\,, \qquad (2.1)$$

where $\boldsymbol{u}$ is the relative Earth-satellite velocity projected onto the plane of the sky, $u_{\perp}$ and $u_{\parallel}$ are the components of $\boldsymbol{u}$ perpendicular and parallel to $\boldsymbol{r}$, and $r = |\boldsymbol{r}|$. In order to derive expressions for $u_{\perp}$, $u_{\parallel}$, and r, we define α as the angle between the source vector $\hat{s}$ and the south ecliptic pole, and ψ as the phase of the orbit such that when $\psi = 0$, the projected displacement vector $\boldsymbol{r}$ is most closely aligned with $\hat{s}$. We define $\Omega_{\oplus} = 2\pi\,\mathrm{yr}^{-1}$, and $R = |\boldsymbol{R}|$ as the magnitude of the Earth-satellite separation vector. The geometry is shown schematically in Figure 1. Using these definitions, we find

$$r = R[1 - \sin^2 \alpha\,\cos^2 \psi]^{1/2}\,,$$

$$u_{\perp} = -\Omega_{\oplus}\,R\,\frac{R}{r}\,\cos \alpha\,, \qquad (2.2)$$

$$u_{\parallel} = -\Omega_{\oplus}\,R\,\frac{R}{r}\,\sin^2 \alpha\,\frac{\sin (2\psi)}{2}\,.$$

Note that in Gould (1995a) the sign of $u_{\parallel}$ was incorrectly given as positive. We now recast the constraint equation in the form

$$\sum_{i=1}^{3} \alpha_i\,a_i = 0\,, \qquad (2.3)$$

where α_i are the coefficients of the constraint, and a_i are the event observables

$$a_i = (\Delta t, \Delta \beta, \Delta \omega)\,. \qquad (2.4)$$

Using this, we find the simplest form for the constraint coefficients is

$$\alpha_i = \left[\Omega_{\oplus}\,\omega\,\sin^2 \alpha\,\frac{\sin (2\psi)}{2},\,\Omega_{\oplus}\,\cos \alpha,\,(1 - \sin^2 \alpha\,\cos^2 \psi)\right].$$
$$(2.5)$$

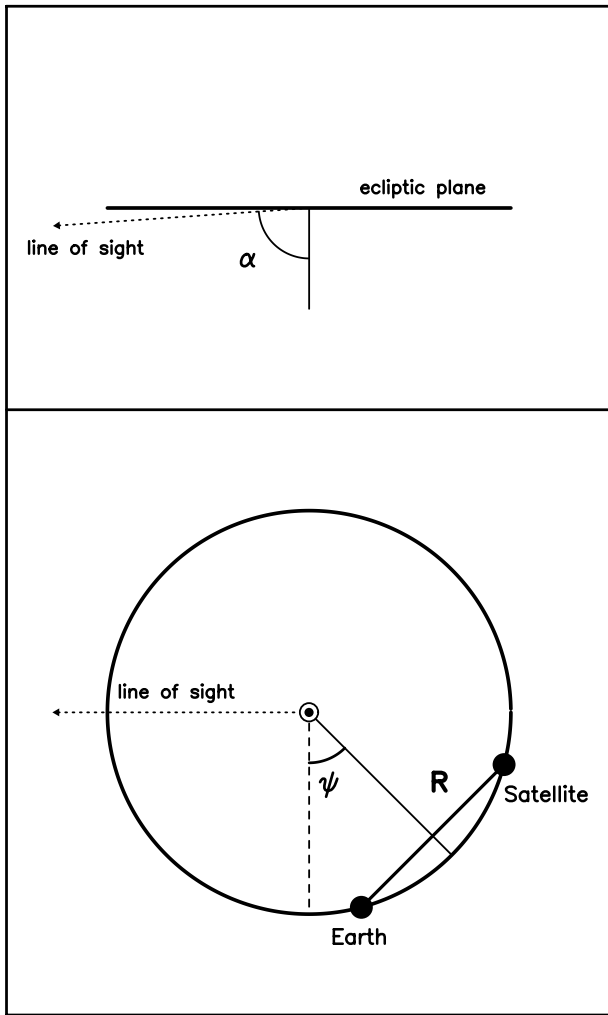In order to break the degeneracy, the constraint equation (2.3) must distinguish between the four degenerate solutions

FIG. 1.—Geometry of the orbits of Earth and the satellite. Note in particular the angle ψ, defined as the angle such that when $\psi = 0$, the projected displacement vector r is most closely aligned with the line of sight.

at the 3 σ level. But, as we have shown above, the constraint coefficients α_i are dependent on α and ψ, the line of sight of observations and the phase of the orbit. Furthermore, from equations (1.3) and (2.2), we see that the vector displacement Δx is a function of α and ψ. Thus, because $\Delta x \equiv (\omega \, \Delta t, \Delta \beta)$, the event observables a_i are also functions of α and ψ. All of these contributions are obviously difficult to disentangle, and thus it is not a straightforward matter to describe the conditions under which the constraint equation (2.3) can break the degeneracy.

2.2. Fractional Error

We define the fractional difference as the difference between the allowed solution and the true solution, divided by the true solution. In order that the degeneracy be broken, we require that the fractional errors in the allowed solutions be less than 10%. The behavior of the fractional errors is easier to understand than the behavior of the constraint. Roughly speaking, as Δx decreases, the fractional errors rise. Thus, from equation (1.3) we can see that as r decreases, or as $\tilde{r}_e$ increases, the fractional errors rise. From

equation (2.2), we see that the projected Earth-satellite separation, r, is a function of direction of the source, α, and the phase of the orbit, ψ. Therefore these parameters affect the fractional error and thereby affect the DBF.

2.3. DBF and Errors

We define the DBF as the fraction of events for which the degeneracy can be broken for a specified set of parameters. We consider that the degeneracy is broken if the difference between all allowed solutions and the true solution is less than 20% of the true solution, and the fractional error in Δx of each allowed solution is less than 10%. In principle, it could be difficult to characterize the errors in the DBF precisely. This is because there are two distinct types of errors that must be considered. The first is an intrinsic error that arises from the uncertainty in the values of each distinct solution. This error is approximately Gaussian distributed. The second error is characterized by two discrete allowed solutions and hence is highly non-Gaussian. Taken together, these errors cannot be described simply.

We would like to be able to characterize our errors as 10% at the 1 σ level. We then consider all possible events with 10% fractional error but with multiple allowed solutions. If two allowed solutions are separated by 20%, then the 1 σ error contour is strongly perturbed by the presence of a second solution, while the 3 σ contour is barely affected. On the other hand, if the discrete solutions are 5% apart, then even the 1 σ contours are essentially unaffected. Thus, at first sight, the threshold for the allowed separations of distinct solutions appears to depend sensitively on the error contour of interest. In practice, however, the DBF is very nearly the same for 5% and 20% thresholds. See Figure 2. In this paper we adopt 20%, which corresponds roughly to focusing on the error contours at the 2 σ level.
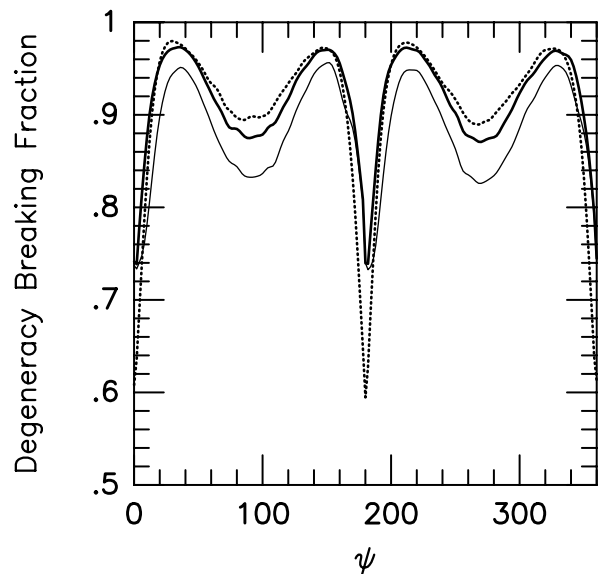

FIG. 2.—Degeneracy breaking fraction (DBF) as a function of ψ for disk-bulge events (*solid bold curve*) and bulge-bulge events (*dashed curve*). All other parameters are fixed at $n_{\rm obs} = 20$, $(\sigma_E, \sigma_S) = (1\%, 2\%)$, $M = 0.3$ $M_\odot$, $d_{\rm sat} = 60°$, $\beta_{\rm max} = 0.7$, and $\alpha = 84°$. DBF is the fraction of events for which the allowed solutions differ by less than 20%, and each of these has intrinsic error less than 10%. Lower solid curve is the DBF as a function of ψ when allowed solutions differ by less than 5%, and each has intrinsic error less than 10%.

2.4. *LMC versus Bulge*

Observations toward the Galactic bulge are markedly different from those toward the LMC. For observations toward the bulge, the results are complicated by the fact that the ability to break the degeneracy is a strong function of the time of year; this is not the case for observations toward the LMC.

For observations toward the LMC, $\alpha \sim 0$, and from equation (2.2) we find $r = R$, $u_{\parallel} = -R\Omega_{\oplus}$, and $u_{\perp} = 0$. These expressions are obviously independent of ψ. Using equation (2.5), the constraint coefficients become $\alpha_i = (0, \Omega_{\oplus}, 1)$. Thus the ability to distinguish between the degenerate solutions is independent of the phase of the orbit and depends only on the photometric precision, the number of observations per crossing time, and the Earth-satellite separation. Given a certain set of parameters, it is therefore possible to quantify the fraction of events for which the degeneracy can be broken, regardless of the phase of the orbit. Furthermore, because r does not vary with ψ, for any given event the fractional errors are also constant throughout the orbit.

The situation is considerably more complicated for bulge observations. For this case, $\alpha \sim 90°$. From equation (2.2), we find that the values of r and $u_{\perp}$ vary as a function of ψ. Therefore the coefficients of the constraint equation (2.5), and hence the ability of the constraint to distinguish between the solutions, are a strong function of the phase of the orbit. For example, consider Baade's window, for which $\alpha = 84°$. For $\psi = 0$ or $180°$, we can approximate the constraint equation as

$$\Delta\beta \simeq -\frac{\Delta\omega}{10\Omega_{\oplus}} , \qquad (2.6)$$

whereas for $\psi = 90°$ or $270°$,

$$\Delta\beta \simeq -\frac{10\,\Delta\omega}{\Omega_{\oplus}} . \qquad (2.7)$$

We can see from these relations the effect of ψ on the ability of the constraint to distinguish between the degenerate values of $\Delta\beta$. For a specified uncertainty in the value of $\Delta\omega$, the uncertainty in $\Delta\beta$ is 100 times less when $\psi = 0$ or $180°$, than when $\psi = 90°$ or $270°$. Thus we can expect that, in general, it is easier to distinguish between the degenerate solutions when $\psi = 0$ or $180°$ than when $\psi = 90°$ or $270°$. For intermediate values of ψ, we can interpolate the behavior of the constraint accordingly.

For bulge observations, the intrinsic errors are also strongly dependent on ψ. From equation (2.2) we see that, for observations near $\alpha = 90°$, the projected Earth-satellite separation, r, varies approximately as $\sin \psi$. Thus, from equation (1.3), for $\psi \sim 0$ or $180°$, the value of Δx is comparatively small, and therefore the fractional errors are comparatively large, whereas for $\psi \sim 90°$ or $270°$, the value of Δx is comparatively large, and thus the fractional errors are comparatively small. As before, we can interpolate the behavior of the fractional errors for intermediate values of ψ.

The effects of ψ on the constraint condition and fractional errors are in competition with each other. We therefore expect the DBF, which is a combination of both of these considerations, to have four minima: when the fractional errors dominate, at $\psi = 0$ or $180°$, *and* when the constraint

on $\Delta\beta$ is poor, at $\psi \simeq 90°$ or $270°$. We expect the maximum values of the DBF to occur where the fractional errors are not dominant, yet the constraint still distinguishes between the degenerate solutions reasonably well. In the next section, we review these qualitative arguments in a more precise form.

3. ERROR ANALYSIS

In this section we give an overview of the mathematical analysis underlying the Monte Carlo code. For a more complete description, we refer the reader to § 2 of Boutreux & Gould (1996); much of the analysis given therein is entirely applicable to the present considerations. The reader who is primarily interested in the results can skip this section entirely.

The flux $F(t)$ from a microlensed star is a function of five parameters, $a_i = (t_0, \beta, \omega, F_0, B)$, with the form,

$$F(t; t_0, \beta, \omega, F_0, B) = F_0 A[x(t; t_0, \beta, \omega)] + B , \quad (3.1)$$

where F_0 is the unlensed flux, and B is the light from any additional unlensed sources that are not resolved. The flux from the satellite can also be described in this manner, by five additional parameters $a_i' = (t_0', \beta', \omega', F_0', B')$. Using measurements simulated by our Monte Carlo method, we then fit the parameters by minimizing χ^2. By differentiating χ^2 in the neighborhood of the solution, one can obtain c_{ij}, the covariance matrix of the a_i for both Earth and the satellite.

We assume that the Earth and satellite have the same filters, implying that $F_0 = F_0'$ and $B = B'$. Each of these constraints can be written $\sum_{i=1}^{10} \alpha_i a_i = 0$, where a_i are now the 10 parameters for Earth and the satellite, and α_i are the constraint coefficients. The constraint coefficients for $F_0 = F_0'$ are $\alpha_i = (0, 0, 0, 1, 0, 0, 0, 0, -1, 0)$. We impose these constraints on the 10×10 covariance matrix c_{ij}, forming a new matrix $\tilde{c}_{ij}$,

$$\tilde{c}_{ij} = c_{ij} - \frac{\sum_{l=1,k}^{10} c_{il}\alpha_l c_{jk}\alpha_k}{\sum_{m,n=1}^{10} c_{mn}\alpha_m\alpha_n} . \qquad (3.2)$$

Neglecting the relative Earth-satellite motion, we find that there is a twofold degeneracy in the magnitude $|\Delta\beta| = \Delta\beta_{\pm}$, and another twofold degeneracy in the sign. Thus there are four possible solutions, $\pm\Delta\beta_{\pm}$. In our simulations, we know the true solution, which for the illustrations given here we take to be $+\Delta\beta_-$ or $(-+)$ for short. However, we initially assume that only the magnitudes of β and β' are known, thus making all four possible values of $\Delta\beta$ equally probable. We use the constrained covariance matrix, $\hat{c}_{ij}$, to form a new covariance matrix of the quantities $a_i = (\Delta t, \Delta\beta, \Delta\omega)$; we call this new matrix c_{ij}^{-+}. Because there are four possible values of $\Delta\beta$, we form four different matrices $c_{ij}^{\pm\,\pm}$. We then test to see if the solutions are distinguishable from the true solution, using the constraint imposed by the relative motion of Earth and the satellite, equations (2.3)–(2.5).

The general form of χ^2 can be written as

$$\chi^2_{-+} = \frac{(\alpha_2\,\delta\beta^{-+})^2}{\sum_{m,n=1}^{3} c_{mn}^{-+}\alpha_m\alpha_n} , \qquad (3.3)$$

where the α_i's are the coefficients from the constraint condition, and $\delta\beta^{-+}$ is the difference between the true and trial values of $\Delta\beta$. Because χ^2 is a strong function of the phase of

the orbit, it is not possible to give χ^2 in a simple form. It is illuminating, however, to examine the form of χ^2 at the values of ψ for which it is at maximum and minimum. For $\psi = (90°, 270°)$, the constraint coefficients are

$$\alpha_i = (0, \Omega_\oplus \cos \alpha, 1) , \qquad (3.4)$$

and for $\psi = (0, 180°)$,

$$\alpha_i = (0, \Omega_\oplus, \cos \alpha) . \qquad (3.5)$$

We define $q = (\sigma_\omega/\sigma_\beta t_e \Omega_\oplus)$, where $\sigma_\omega = c_{33}^{1/2} t_e$ and $\sigma_\beta = c_{22}^{1/2}$. Using these expressions, and assuming (as is generally the case), that the off-diagonal covariances ($c_{ij}, i \neq j$) are small, the equation for χ^2 can be written for each case as

$$\chi^2_{\min} = \chi^2(90°, 270°) = \frac{\delta\beta/\sigma_\beta}{1 + (q/\cos \alpha)^2} ,$$
$$\qquad (3.6)$$
$$\chi^2_{\max} = \chi^2(0, 180°) = \frac{\delta\beta/\sigma_\beta}{1 + (q \cos \alpha)^2} .$$

For typical events, $q \sim 6$ for the $\pm\Delta\beta_-$ solutions; this value is roughly independent of ψ.

Note that $\chi^2_{\min}/\chi^2_{\max} \sim (\cos \alpha/q)^2$ (for typical timescales). Thus for observations toward the bulge, $\alpha \simeq 84°$, χ^2 can vary by a factor of 10^2–10^4 over the course of the orbit.

We calculate the χ^2 for all four solutions, and consider only those solutions for which $\chi^2 \leq 9$. We then calculate the intrinsic error for these allowed solutions. The fractional error in the scalar solution can be approximated by $\langle(\delta \Delta x)^2\rangle^{1/2}/\Delta x$, where again $\Delta x \equiv (\omega \Delta t, \Delta\beta) = (a_1, a_2)$, and $\Delta x = |\Delta x|$. Using the analog of equation (3.2),

$$\tilde{c}_{ij}^{-+} = c_{ij}^{-+} - \frac{\sum_{l=1,k}^{3} c_{il} \alpha_l c_{jk} \alpha_k}{\sum_{m,n=1}^{3} c_{mn} \alpha_m \alpha_n} , \qquad (3.7)$$

we apply the constraint (2.3) to c^{-+} to form $\tilde{c}^{-+}$, where α_i is now given by equation (2.5), and $a_i = (\Delta t, \Delta\beta, \Delta\omega)$. In terms of $\tilde{c}_{ij}^{-+}$, the fractional error becomes

$$\frac{\langle(\delta \Delta x)^2\rangle^{1/2}}{\Delta x} = \frac{(\sum_{i,j=1}^{2} \tilde{c}_{ij}^{-+} a_i a_j)^{1/2}}{(a_1)^2 + (a_2)^2} . \qquad (3.8)$$

From this we can see that as the quantities (a_1, a_2) become small, the fractional error in the solutions rise. Recall that for $\psi \sim 0$, the projected Earth-satellite separation is small (relative to the true separation), and therefore Δx is small. Thus the intrinsic errors in the solutions become more important near $\psi = 0$.

We approximate the fractional error in the vector solution by $\langle(\delta \Delta x)^2\rangle^{1/2}/\Delta x$. This can be written as

$$\frac{\langle(\delta \Delta x)^2\rangle^{1/2}}{\Delta x} = \left[\frac{\tilde{c}_{11}^{-+} + 2\tilde{c}_{12}^{-+} + \tilde{c}_{22}^{-+}}{(a_1)^2 + (a_2)^2}\right] . \qquad (3.9)$$

4. BULGE AND DISK MODELS

In order to calculate the DBF using the Monte Carlo simulation, we adopt appropriate models for the velocity and density distributions of the disk and bulge of the Milky Way.

For the density distributions, we choose a Bahcall model for the disk. For the bulge, we adopt a "revised" COBE model. This model uses a barred bulge density distribution

for the outer parts of the bulge ($r > 0.7$ kpc) and a Kent model for the inner part of the bulge. For a more detailed description, see Table 3 from Han & Gould (1995).

We assume the velocity distributions to be Gaussian, with mean velocity $\bar{v}$, and velocity dispersion σ. For the disk, we use $(\bar{v}_x, \bar{v}_y, \bar{v}_x) = (0, 220, 0)$; with dispersions of $(\sigma_x, \sigma_y, \sigma_z) = (40, 30, 20)$ km s^{-1}. For the bulge, $(\bar{v}_x, \bar{v}_y, \bar{v}_x) = (0, 0, 0)$, while $(\sigma_x, \sigma_y, \sigma_z) = (110, 82.5, 66.3)$ km s^{-1}. The motion of the Sun is also taken into account, and is $(v_x, v_y, v_z) = (9, 231, 16)$ km s^{-1} (Mihalas & Binney 1981).

There are two distinct types of events that are seen toward the bulge. These are bulge-bulge events, where a bulge star is being lensed by bulge lens, and disk-bulge events, where a bulge star is being lensed by a disk lens. These two situations produce dissimilar events, and we therefore consider them separately.

For disk-bulge events, the position of the source star, d_{os}, is confined to a relatively narrow range as compared to the range of possible values for d_{ol}. Thus we can approximate the location of the source stars as being fixed at the galactocentric radius, $R_0 = 8$ kpc. The frequency of lensing events scales as $\rho(r_l)r_e v \propto \rho(r_l)[z(1-z)]^{1/2}v$, where v is the transverse velocity of the lens, r_l is the distance of the lens from the Galactic center (for lines of sight near the Galactic center, $r_l \simeq d_{ls}$), and $\rho(r_l)$ is the mass density at r_l. Thus to simulate an event, we draw the distance to the lens randomly from the probability distribution $\rho(r_l)[z(1-z)]^{1/2}$. The velocities of the lens and the source are then drawn randomly according to the parameters described above, and the transverse velocity calculated. We weight the DBF by the transverse speed in order to include its effect on the event rate.

For bulge-bulge events, the frequency of lensing events depends on the mass density at the position of the source, the mass density at the position of the lens, the size of the Einstein ring, and the transverse velocity of the lens. In addition, as the distance from the observer increases, the volume element along the line of sight also increases, and therefore so does the total number of stars. Thus the event rate scales as $\rho(r_s)\rho(r_l)r_e d_{os}^2 v$. Here r_s is the distance of the source from the Galactic center, and d_{os}^2 provides the contribution due to the increasing volume element. Thus, the source-lens pair position (d_{os}, d_{ol}) is drawn randomly from the distribution $\rho(r_s)\rho(r_l)[z(1-z)]^{1/2}d_{os}^2$. The resulting DBF is weighted by the transverse velocity, as above.

5. MONTE CARLO

For the simulation, we assume that the observations begin when the source enters the Einstein ring radius as seen from Earth. The observations continue until the source-lens separation is $\geq 3r_e$ as seen from both Earth and the satellite. The impact parameter, β, is either fixed, or chosen randomly in the range $0 < \beta < 0.7$. This range of β is consistent with that of observed microlensing events. Those events for which the time of maximum magnification for the satellite has already passed when the observations begin, that is, $(1 - \beta^2)^{1/2} < \omega \Delta t$, are considered unresolvable. Those events for which $\beta' > 1.5$ are also considered unresolvable.

The four possible solutions are considered separately, and the χ^2 calculated for each. Those solutions for which $\chi^2 > 9$ are distinguishable from the true solution and are therefore unallowed. We then determine if the allowed solutions are sufficiently similar that it is unimportant to break

the degeneracy, and if the fractional errors in the solutions are intolerably large. The scalar difference between the solutions is given by

$$\delta(\Delta x) = |\Delta x|_{\text{allowed}} - |\Delta x|_{\text{true}} , \qquad (5.1)$$

whereas the vector difference is given by

$$\delta(\Delta x) = |\Delta x_{\text{allowed}} - \Delta x_{\text{true}}| . \qquad (5.2)$$

If the difference between all allowed solutions and the true solution is less than 20% of the true solution, and if the fractional error in Δx of each allowed solution is less than 10%, we consider that the degeneracy is broken. For each set of parameters, the Monte Carlo simulation was run 5000 times, resulting in errors of less than 1%.

6. OBSERVATIONAL CONSIDERATIONS

Because the bulge is located at ecliptic angle $\alpha \sim 90°$, there will be times of the year that observations will be impossible, due to the position of the Sun. To quantify this effect, we define an allowed range of the ecliptic longitude, Λ, for the Earth and the satellite. When the position of Earth or the satellite is within this range, observations are considered impossible. The full width of this range is chosen to be 90° (3 months) for Earth, and 60° (2 months) for the satellite. In our simulations, we consider lines of sight toward the bulge, for which $\Lambda = 270°$. The forbidden ranges for Earth and satellite are then

$$90° - 45° \leq \Lambda_E \leq 90° + 45° ,$$

$$90° - 30° \leq \Lambda_S \leq 90° + 30° . \qquad (6.1)$$

Note that $\Lambda = 0$ is the vernal equinox. The time of the year when either Earth or the satellite is within the forbidden range is dependent on the Earth-satellite separation, d_{sat}. For $d_{\text{sat}} \leq 75°$, the forbidden ranges of Earth and satellite overlap. Conversely, for $d_{\text{sat}} \geq 75°$, the forbidden ranges are separated by a gap of $\Delta\Lambda = d_{\text{sat}} - 75°$. Thus values of $d_{\text{sat}} \geq 75°$ are somewhat less desirable due to the fact that the times of year when observations are possible are separated into two ranges, thereby increasing the probability that the observations of an event will be foreshortened due to Earth or the satellite moving behind the Sun. We will consider this issue more fully in § 7.1, when we discuss the optimal Earth-satellite separation.

7. RESULTS

There are eight parameters that affect the degeneracy breaking fraction; α, the angle between the source and the south ecliptic pole; ψ, which is related to the phase of the orbit; σ_E and σ_S, the photometric precisions of the Earth and satellite observations, respectively; β, the impact parameter as seen from Earth; d_{sat}, the Earth-satellite separation distance; M, the mass of the lens; N_{meas}, the number of measurements per Einstein ring crossing time.

For all of the parameters (neglecting ψ for the moment), we choose typical values that we consider to be realistic. These values are used in all simulations unless varied explicitly. A value of $N_{\text{meas}} = 20$ corresponds to frequency of measurements in the range of 0.5 to 4.0 days for typical events. We choose $(\sigma_E, \sigma_S) = (1\%, 2\%)$ as our photometric precision. The photometric precision obviously depends on the

magnitude of the source star; these are typical values of photometric precision for giant sources. We choose $M = 0.3\ M_\odot$ as a representative mass of lenses for observations toward the bulge. The default Earth-satellite separaion is $d_{\text{sat}} = 60°$ (2 months). The maximum impact parameter is set at $\beta_{\text{max}} = 0.7$. For Baade's window, $\alpha = 84°$.

Observations toward the bulge are unique in that they are a strong function of the time of year, as discussed above. Due to this intrinsic dependence of the DBF on ψ, we include ψ as a free parameter in all further calculations.

In order to elucidate the effect of the time of the year on the DBF, we present in Figure 2 the DBF against ψ for our fiducial parameters. Included in Figure 2 are the results for both the disk-bulge and bulge-bulge cases. Also included is the DBF against ψ for a fractional difference threshold of 5% (see § 2.3). Within the limits of the Monte Carlo errors, we find that in the range $0 \leq \psi \leq 180°$ the curve is equivalent to that for the range $180° \leq \psi \leq 360°$. We utilize this symmetry by restricting the range of ψ in further calculations to $0 \leq \psi \leq 180°$. There is, however, a slight asymmetry around $\psi = 90°$ (and similarly around $\psi = 270°$). For the speed degeneracy, this asymmetry makes no significant contribution, and we disregard it. We will consider this effect more fully in § 8, where we discuss the velocity degeneracy. For $\psi \sim 0, 180°$, we see from equation (2.2) that the projected Earth-satellite velocity is at a maximum, and as a result the constraint given in equation (2.1) is very effective in distinguishing between the possible solutions. The projected Earth-satellite separation is at a minimum, however, driving up the fractional errors in the solutions. Thus near $\psi \sim 0, 180°$, the DBF is dominated by the intrinsic errors. As ψ increases, the projected Earth-satellite velocity decreases as ψ increases, and as a result the constraint becomes less effective in distinguishing between the degenerate solutions. For $\psi \simeq 20°$ the DBF is at a maximum; the constraint still distinguishes between the solutions for a majority of the events, while the intrinsic errors are typically $\leq 10\%$. When $\psi = 90°$, the projected Earth-satellite separation is equal to the true Earth-satellite separation, and the intrinsic errors are typically $\leq 5\%$. The projected Earth-satellite velocity is at a minimum at $\psi = 90°$, and the constraint distinguishes poorly among the solutions (as compared to $\psi \sim 0$). Thus, at $\psi = 90°$, the DBF is dominated by the difficulty in distinguishing between the individual solutions. The analysis of the DBF curve in the range $0 \leq \psi \leq 90°$ is identical to that for the rest of the orbit.

The analysis of bulge-bulge events is exactly the same as for disk-bulge events. We can understand how disk-bulge and bulge-bulge events differ by considering the typical size of the projected Einstein ring in each case. For disk-bulge events, the median value for the distance to lens is $d_{ol} \sim 5$ kpc, and the distance to the source is $d_{os} = 8$ kpc, thus, from equations (1.2) and (1.4), we find that, for disk lenses, $\tilde{r}_e \simeq 6.0\text{AU}(M/0.3\ M_\odot)^{1/2}$. For bulge-bulge events, $d_{ol} \sim 7$ kpc, $d_{os} \sim 9$ kpc, so that $\tilde{r}_e \simeq 9.0\text{AU}(M/0.3\ M_\odot)^{1/2}$. Therefore the typical size of the projected Einstein rings will be larger for bulge-bulge events by a factor of ~ 1.5. This will affect the value of the DBF in two distinct ways. For phases of the orbit such that $\psi \sim 0$, where intrinsic errors dominate, the DBF for bulge-bulge events will be smaller than that for disk-bulge events, due to the larger typical values of $\tilde{r}_e$ (and therefore larger fractional errors). For phases of the orbit such that $\psi \sim 90°$, we expect that the DBF for bulge-bulge

events will be, in general, higher than the corresponding DBF for disk-bulge events, due to the fact that the degenerate $\Delta\beta$ solutions are better separated in the case of the bulge-bulge events than those for disk-bulge events.

For disk-bulge events, we find that, for our fiducial parameters, it is possible to resolve greater than 87% of the events during most times of the orbit, and greater than 70% of the events over the entire orbit. For bulge-bulge events, we find values of greater than 90% for most of the orbit and greater than 60% for the entire orbit.

Figure 3 represents the DBF as a function of ψ and β for disk-bulge events. For this figure, β is not randomly chosen, but rather held fixed for each point in the curve. Contrary to the results for the LMC (Boutreux & Gould 1996), where it was found that events with $\beta \geq 0.7$ are much harder to resolve, there is no one value of β for which the DBF drops below a certain value. In fact, for $\psi = 90°$, even those events for which $\beta \sim 0.9$ are resolvable 80% of the time, whereas less than 20% of these events are resolvable when $\psi = 10°$. In other simulations, we choose β randomly between $0 \leq \beta \leq 0.7$ because the majority of events seen so far have values of β that are in this range, but we emphasize that, under the proper conditions, even those events that have $\beta > 0.7$ may still be resolvable.

Figure 4 represents the DBF as a function of ψ and M for disk-bulge events. For the mass, we focus on the range 0.01–1 $M_\odot$; this corresponds to the best estimate of the range of masses for events already observed. For our fiducial value, $M = 0.3\ M_\odot$, the DBF is $\sim 90\%$ for the majority of the orbit. For disk-bulge events, the projected Einstein ring radius is $\tilde{r}_e \simeq 6.0\mathrm{AU}(M/0.3\ M_\odot)^{1/2}$. Consider first phases of the orbit for which $\psi \sim 0$, where the fractional errors dominate the behavior of the DBF. For these values of ψ (and $R \sim 1\mathrm{AU}$), the projected Earth-satellite separation is $r \sim 0.1\mathrm{AU}$. The fractional errors become important when $\Delta x \ll 1$. A quick calculation shows that, for masses greater than $M \geq 0.1\ M_\odot$, the magnitude of the vector dis-
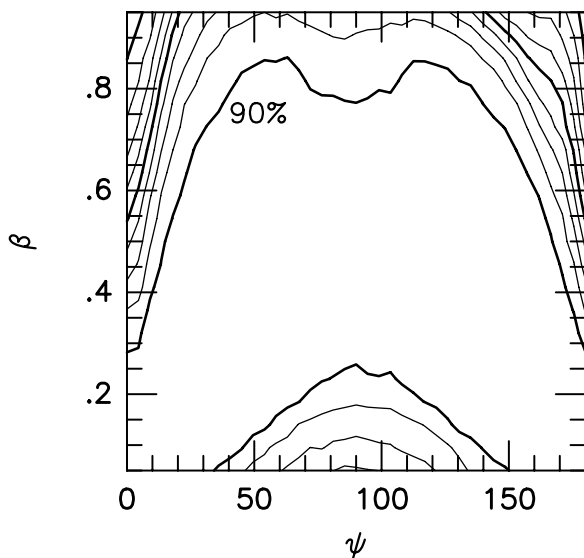
placement is $\Delta x = r/\tilde{r}_e < 0.1$, and thus the fractional errors begin to dominate, thereby lowering the DBF. For masses $M \leq 0.03\ M_\odot$, $\Delta x = r/\tilde{r}_e \sim 1$, and thus the fractional errors are unimportant, and the DBF is greater than 90%. Consider now phases of the orbit for which $\psi \sim 90°$. For the range of masses considered here, $\Delta x \geq 1$, and thus the fractional errors are never large. Considering increasingly smaller masses, we find that more of the events are unresolvable, due to the fact that the projected Earth-satellite separation, r, becomes increasingly larger than the Einstein ring radius, $\tilde{r}_e$, and the event as seen from the satellite will more frequently fall outside of the Einstein ring. Thus the DBF drops rapidly from 90% to 40% from $M = 0.3\ M_\odot$ to $M = 0.03\ M_\odot$.

Figure 5 represents the DBF as a function of ψ and B, the ecliptic latitude ($B = \alpha - 90°$), for disk-bulge events. For this figure, we hold the ecliptic longitude fixed at $\Lambda = 270°$,

FIG. 4.—DBF as a function of ψ and $\log M/M_\odot$ for disk-bulge events. Contours are the same as those in Fig. 3.

FIG. 3.—DBF as a function of ψ and β for disk-bulge events. Labeled bold contour represents a DBF of 90%. Other bold contours represent DBFs of 50% and 10%. Intermediate contours are spaced at intervals of 10%. All other parameters are held fixed at our fiducial parameters, as in Fig. 2.
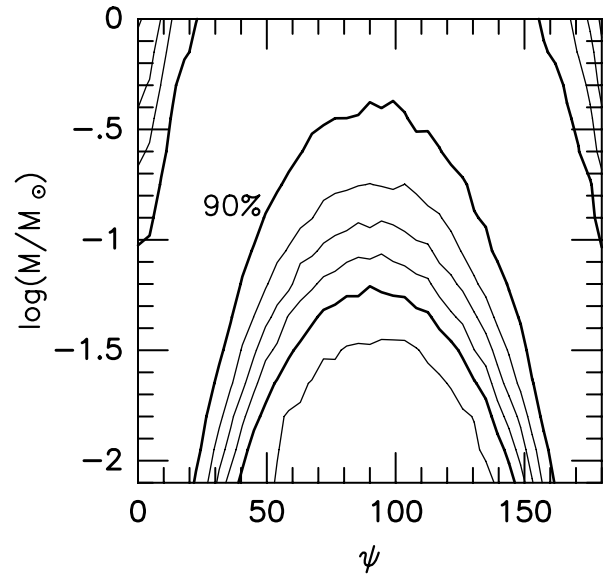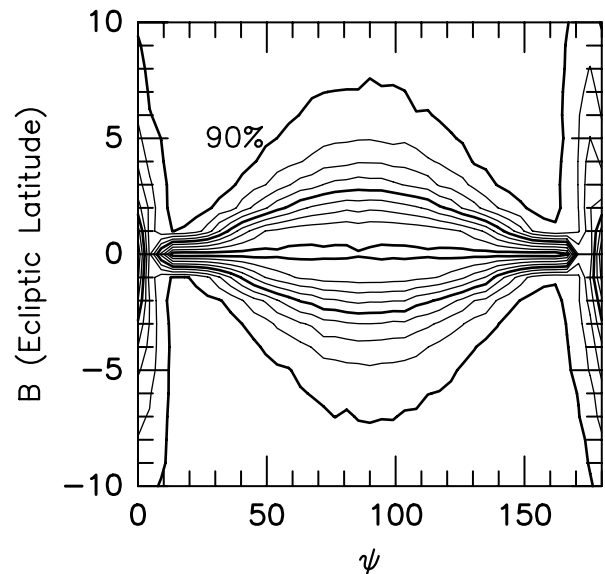

FIG. 5.—DBF as a function of ψ and B for disk-bulge events. Contours are the same as those in Fig. 3.

and vary B in the range $-10° \leq B \leq 10°$. In galactic coordinates, this corresponds to the range $(l, b) = (-2°, -5°) - (16°, 4°)$. For Baade's window, $B = -6°$, the DBF is greater than 90% for the entire orbit. Note that for $B = 0$, it is impossible to break the degeneracy. This is due to the fact that, at $B = 0$, the constraint given in equation (2.1) becomes $\sum_{i=i}^{3} \alpha_i a_i = \Delta\omega + \Omega_\oplus \omega \Delta t \cot \psi = 0$, and thus does not constrain the value of $\Delta\beta$ at all. Similarly, for small values of $|B|$, the value of $\Delta\beta$ is poorly constrained. Thus, there is a range of ecliptic latitude, $|B| < 1°$, where the DBF is less than 40% for a majority of the orbit; this range should be avoided when making observations. Lines of sight where $|B| > 2°$ are optimal.

Figure 6 represents the DBF as a function of ψ and $d_{\rm sat}$, the Earth-satellite separation, for disk-bulge events. Also shown is the range of ψ for which observations are impossible due to the position of the Sun. This range is a function of $d_{\rm sat}$; thus by considering simultaneously how this range and the DBF vary as function of $d_{\rm sat}$, we can find an optimal Earth-satellite separation. For $d_{\rm sat} \leq 30°$, the range where observations are impossible is smallest ($\sim 90°$), but the DBF is never greater than 80%. For $d_{\rm sat} = 60°$, the observationally forbidden range is only slightly larger ($\sim 130°$), and the DBF is greater than 90% for the majority of the orbit. For $d_{\rm sat} > 75°$, the forbidden ranges for Earth and the satellite begin to diverge, and the times of the orbit where observations are possible become separated. Thus, although the DBF continues to improve as $d_{\rm sat}$ increases, there is an increased likelihood for these ranges that an observation will be foreshortened due to Earth or the satellite moving behind the Sun. We consider $20°–75°$ to be the optimal range for the Earth-satellite separation. For $d_{\rm sat} < 20°$, the DBF is unacceptably low.

We also considered the dependence of the DBF on the parameters β, M, B, and $d_{\rm sat}$ for bulge-bulge events. We find the results to be almost identical to those for disk-bulge events, with variations of at most $\sim 10\%$, when the phase of the orbit is $\psi \sim 0$ or $180°$, but typically the variations are much smaller. For reasons discussed above, the DBF is, in general, somewhat higher when $\psi \sim 90°$, and somewhat lower when $\psi \sim 0$ for bulge-bulge events. As with disk-bulge events, we find that there is no natural cutoff value for β; for our fiducial value of $M = 0.3\ M_\odot$, the DBF is $\sim 90\%$ for the majority of the orbit; for Baade's window, $B = -6°$, the DBF is greater than 90% for the majority of the orbit; and the optimal range of $d_{\rm sat}$ is $20°–75°$. Overall, the differences between bulge-bulge and disk-bulge events are minor, and will not significantly affect the observations.

8. THE VELOCITY DEGENERACY

In the previous section, we discussed the observational requirements of a satellite to break the twofold degeneracy in the projected speed, $\tilde{v}$. While measuring the projected speed is helpful in distinguishing between component populations, a measurement of the projected velocity, $\tilde{v}$, would provide a more conclusive distinction.

In this section we present the results for breaking the fourfold velocity degeneracy, adopting the fiducial parameters used in the previous section: $N_{\rm meas} = 20$, $(\sigma_E, \sigma_S) = (1\%, 2\%)$, $M = 0.3\ M_\odot$, $d_{\rm sat} = 60°$ (2 months), $\beta_{\rm max} = 0.7$, and $\alpha = 84°$. We calculate the difference between the allowed solutions using equation (5.2), and the fractional error in each allowed solution using equation (3.9). As in the previous section, if the intrinsic errors in all allowed solutions is less than 10%, and if the difference between the allowed solutions is less than 20% of the true solution, we consider the degeneracy to be broken. Here we present the results for both disk-bulge and bulge-bulge type events.

Figure 7 represents the vector DBF as a function of ψ for disk-bulge events and bulge-bulge events. The scalar DBF is also shown for comparison. We find that for disk-bulge events the DBF is greater than $\sim 40\%$ for the entire orbit, and greater than $\sim 55\%$ for about half the orbit. We find that for bulge-bulge events the vector DBF is $\gtrsim 30\%$ over the entire orbit, and $\gtrsim 40\%$ over half the orbit. In general, the analysis of the vector DBF curve is the same as that for
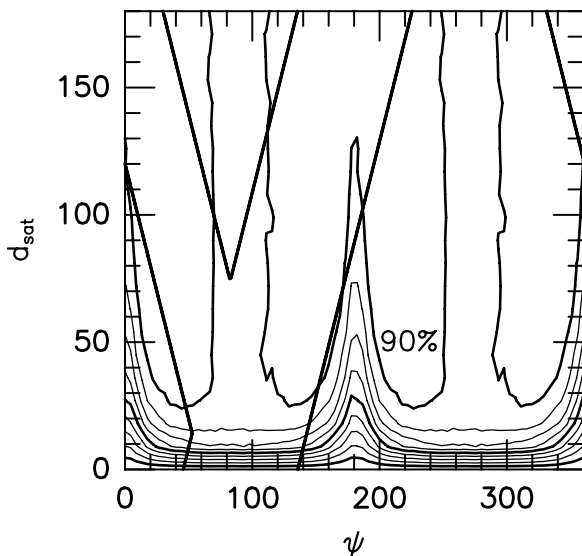

FIG. 6.—DBF as a function of ψ and $d_{\rm sat}$ for disk-bulge events. The y-shaped area of the graph between the heavy lines represents the range of ψ for each value of $d_{\rm sat}$ where observations are impossible due to the position of the Sun. The other contours are the same as those in Fig. 3.
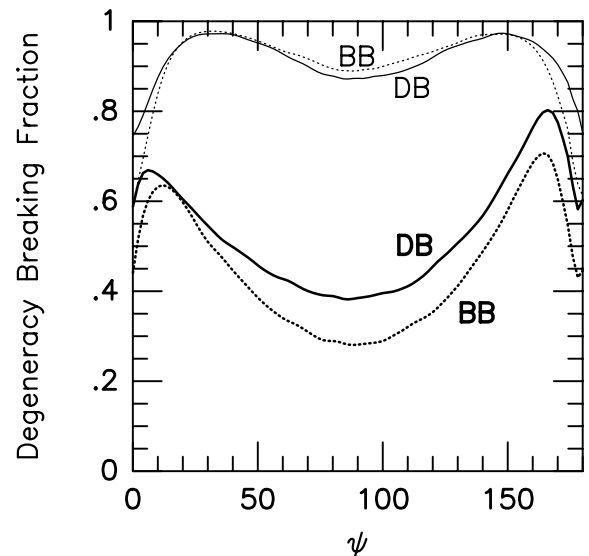

FIG. 7.—Vector DBF as a function of ψ for disk-bulge events (*bold solid curve*) and for bulge-bulge events (*bold dashed curve*). Also shown is the corresponding scalar DBF. All other parameters are fixed at $n_{\rm obs} = 20$, $(\sigma_E, \sigma_S) = (1\%, 2\%)$, $M = 0.3\ M_\odot$, $d_{\rm sat} = 60°$, $\beta_{\rm max} = 0.7$, and $\alpha = 84°$.

scalar DBF curve: there are minima at $\psi = 0$ and $180°$ where the intrinsic errors dominate the DBF, and a minimum at $\psi = 90°$ where the ability of the constraint to distinguish between the degenerate solutions dominates the DBF. There are two unique features of the vector DBF, however. The first is that the minimum value of the DBF occurs at $\psi \sim 90°$, where the limiting factor is the ability to distinguish between the solutions. In the scalar case, distinguishing between the $\pm \Delta\beta_-$ solution is unimportant, due to the fact that these solutions are essentially the same. To break the vector degeneracy, however, one must distinguish between the $\pm \Delta\beta_-$ solutions, which is often difficult when $\psi \sim 90°$, where the constraint is the least effective. We also find a significant asymmetry in the vector DBF curve around $\psi = 90°$, the largest asymmetry being a difference of $\sim 15\%$ between the DBF at $\psi = 15°$ and $165°$. This asymmetry is caused by fact that lenses in the disk have a preferred direction of motion, and, to a lesser extent, from the motion of the Sun around the Galactic center. For a given event, $\Delta\beta \propto \tilde{v}_\perp$, where $\tilde{v}_\perp$ is the component of the transverse velocity perpendicular to the projected Earth-satellite separation, r. As ψ changes, the direction perpendicular to the projected Earth-satellite separation, r. As ψ changes, the direction perpendicular to r changes with respect to the preferred direction of disk. Thus a preferred direction for $\tilde{v}$ will translate into an asymmetry in the distribution of values of $\Delta\beta$ around $\psi = 90°$. Specifically, the values of $\Delta\beta$ are typically smaller when $\psi < 90°$ than when $\psi > 90°$. Therefore, because the $\pm\Delta\beta_-$ solutions are, on average, more closely spaced when $\psi < 90°$, the constraint is less likely to distinguish between them, and the DBF is smaller. This asymmetry does not arise in the scalar DBF curve because it is not necessary to distinguish between the $\pm\Delta\beta_-$ solutions. Note the smaller asymmetry around $\psi = 90°$ for bulge-bulge events. This is due to the fact that, in bulge-bulge events, there is no preferred direction of motion of the lens as there is in disk-bulge events.

APPENDIX

GENERALIZED SATELLITE ORBITS

For our Monte Carlo simulations, we assumed that the satellite is in an Earth-like orbit, and that both the orbit of Earth and the orbit of the satellite are circular. In reality, a satellite launched from Earth will not be in an Earth-like orbit, but will actually be in an elliptical orbit. This implies that the true velocity of the satellite will differ from the assumed velocity for each value of the Earth-satellite separation. In this Appendix, we show that, for a reasonably small deviation from a circular orbit, the difference between the true and assumed Earth-satellite velocity will be small, and that therefore our results are sufficiently generic to be applicable to a large class of orbits.

When launched from Earth, the satellite will have some velocity with respect to Earth. We assume the direction of the satellite's velocity is parallel to that of Earth (i.e., the orbit of the satellite is in the plane of Earth's orbit, and the satellite's perihelion is at the distance of Earth). That is, $v_{\mathrm{sat}} = v_\oplus + \delta v$. We assume that the orbit of Earth is circular; therefore, a nonzero value of δv implies that the satellite will have an elliptical orbit with a period different from that of Earth's and it will
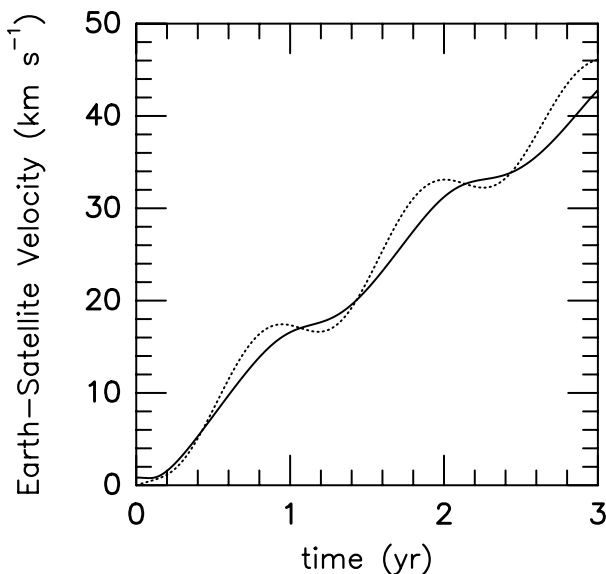

FIG. 8.—Earth-satellite velocity as a function of time from launch. Shown are the Earth-satellite velocity assuming a circular orbit (*dotted line*), and the real Earth-satellite velocity (*solid line*).

drift away from Earth over time. Using Kepler's laws, one finds that the difference between the period of Earth and the satellite is given by

$$\frac{\delta P}{P_\oplus} = \frac{3\,\delta v}{v_\oplus}\;.$$

(A1)

In § 8.2, we determined that the optimal Earth-satellite separation was in the range $20°–75°$, or $\frac{2}{3}$ month–$2\frac{1}{2}$ months. We would like the Earth-satellite separation to vary in this range over the course of ~ 3 yr. For definiteness, we choose the Earth-satellite separation to be 3 months after 3 yr, i.e., $\delta P/P_\oplus \sim 1/12$. Thus, from equation (A1), and using $v_\oplus = 30$ km s^{-1} we find $\delta v \sim 0.8$ km s^{-1}. The orbit is nearly circular, with an eccentricity of $e = 0.06$.

Using the parameters of the orbit, we can now calculate the difference between the true value of the Earth-satellite velocity and the value used in our simulation (which assumed a circular, Earth-like orbit for the satellite). We set $t = 0$ as the time of launch, and at each point in time, we calculate the true Earth-satellite separation and velocity. We then calculate what the value of the Earth-satellite velocity would be if the satellite were in an Earth-like orbit, separated from the Earth by an amount equal to the true Earth-satellite separation. This corresponds to the velocity used in our Monte Carlo code. Figure 8 shows the Earth-satellite velocity for both cases in the range $0 \le t \le 3$ yr. Focusing on $t > 0.5$ yr, we find that the true velocity is systematically smaller than the assumed velocity by $\sim 6\%$, but varies from being $\sim 18\%$ smaller to $\sim 6\%$ larger.

Here we have calculated the difference between the true Earth-satellite velocity and that assuming an Earth-like orbit for the satellite. For the purposes of degeneracy breaking, however, it is the projected Earth-satellite velocity that is important. In the case of an elliptical orbit, the magnitude of the projected Earth-satellite velocity is dependent on the time of year in which the satellite is launched. Since we do not know a priori when this will be, we cannot find precisely the difference between the true and assumed projected Earth-satellite velocity. This is not strictly necessary, however, since the difference between the projected velocities will be of the same order as the difference between the space velocities. Since the ability to break the degeneracy is roughly proportional to the projected Earth-satellite velocity, we conclude that the error introduced in our simulation by assuming an Earth-like orbit for the satellite is of order the error in the Earth-satellite velocity, $\sim 6\%$.

We conclude that the results obtained in our simulations are applicable to likely satellite orbits. If, however, one would like to consider satellite orbits that are either highly inclined to Earth's orbit, or highly eccentric, then our results are not applicable. These situations will need to be analyzed individually.

REFERENCES

Alard, C. 1996, in IAU Symp. 173, Astrophysical Applications of Gravitational Lensing, ed. C. S. Kochanek & J. N. Hewitt (Dordrecht: Kluwer), 215
Alcock, C., et al. 1995a, ApJ, 445, 133
———. 1995b, ApJ, 449, 28
———. 1995c, ApJ, 454, L125
———. 1996a, ApJ, submitted
———. 1996b, ApJ, 461, 84
Ansari, R., et al. 1996, A&A, in press
Aubourg, E., et al. 1995, A&A, 301, 1
Bahcall, J. N., Flynn, C., Gould, A., & Kirhakos, S. 1994, ApJ, 435, L51
Boutreux, T., & Gould, A. 1996, ApJ, 462, 705
Gould, A. 1994, ApJ, 421, L71
———. 1995a, ApJ, 441, L21
Gould, A. 1995b, ApJ, 441, 77
———. 1996, PASP, 108, 465
Gould, A., Bahcall, J. N., & Flynn, C. 1996, ApJ, 465, 759
Gould, A., & Welch, D. 1996, ApJ, 464, 212
Griest, K. 1991, ApJ, 366, 412
Han, C., & Gould, A. 1995, ApJ, 447, 53
Loeb, A., & Sasselov, D. 1995, ApJ, 449, L33
Maoz, D., & Gould, A. 1994, ApJ, 425, L67
Mihalas, D., & Binney, J. 1981, Galactic Astronomy (New York: Freeman)
Nemiroff, R. J., & Wickramasinghe, W. A. D. T. 1994, ApJ, 424, L21
Paczyński, B. 1986, ApJ, 304, 1
Udalski, A., et al. 1994, Acta Astron., 44, 165
Witt, H. 1995, ApJ, 449, 42
Witt, H., & Mao, S. 1995, ApJ, 430, 505